01 Jan 2010

Direct Detection Of NO Produced By High-temperature Surface-catalyzed Atom Recombination

Dušan A. Pejaković

Jochen Marschall

Lian Duan
Missouri Unviersity of Science and Technology, duanl@mst.edu

Maria P. Martin

Recommended Citation

D. A. Pejaković et al., "Direct Detection Of NO Produced By High-temperature Surface-catalyzed Atom Recombination," *Journal of Thermophysics and Heat Transfer*, vol. 24, no. 3, pp. 603 - 611, American Institute of Aeronautics and Astronautics, Jan 2010.
The definitive version is available at https://doi.org/10.2514/1.47175

JOURNAL OF THERMOPHYSICS AND HEAT TRANSFER
Vol. 24, No. 3, July–September 2010

Direct Detection of NO Produced by High-Temperature Surface-Catalyzed Atom Recombination

Dušan A. Pejaković* and Jochen Marschall†
SRI International, Menlo Park, California 94025
and
Lian Duan‡ and Maria P. Martin§
Princeton University, Princeton, New Jersey 08544

DOI: 10.2514/1.47175

The surface-catalytic recombination of oxygen and nitrogen atoms to form nitric oxide was confirmed by the direct detection of product NO molecules, using single-photon laser-induced fluorescence spectroscopy. Experiments were performed from room temperature to 1200 K in a quartz diffusion-tube sidearm reactor enclosed in a high-temperature tube furnace. Atomic nitrogen was generated using a microwave discharge, and atomic oxygen was produced via the rapid gas-phase titration reaction $N + NO \rightarrow O + N_2$. The use of isotopically labeled titration gases $^{15}N^{16}O$ and $^{15}N^{18}O$ allowed for the unambiguous identification of nitric oxide produced by the O + N surface reaction. The absolute number densities of surface-produced NO were determined from separate calibration experiments using $^{14}N^{16}O$. Observed variations of the NO number density with temperature and varying O/N atomic ratios at the sidearm entrance are generally consistent with the predictions of a simple reaction-diffusion model of the sidearm reactor that includes surface-catalyzed NO production as a species boundary condition.

Nomenclature

c	=	concentration or molar density, mol m^{-3}
D	=	diffusion coefficient, m^2 s^{-1}
E	=	activation energy, J mol^{-1}
$f_{s,r}$	=	branching fraction of reactant s into product r
j	=	diffusive mass flux, kg m^{-2} s^{-1}
k_i	=	rate coefficient for reaction i, cm^3 molecule^{-1} s^{-1} or cm^6 molecule^{-2} s^{-2}
L	=	sidearm length, m
M	=	molar mass, kg mol^{-1}
P	=	pressure, Pa
R	=	sidearm radius, m
$\Re$	=	universal gas constant, 8.314 J mol^{-1} K^{-1}
r	=	radial sidearm coordinate, m
T	=	temperature, K
$\bar{v}$	=	average thermal speed, m s^{-1}
w	=	gas-phase production rate, kg m^{-3} s^{-1}
w_w	=	surface production rate, kg m^{-2} s^{-1}
x	=	mole fraction
z	=	axial sidearm coordinate, m
γ	=	loss probability
ρ	=	mass density, kg m^{-3}
υ	=	diffusion velocity, m s^{-1}

Subscripts

O, O_2, N, N_2, NO	=	species
r	=	species index or radial direction
s	=	species index
w	=	wall
z	=	axial direction

I. Introduction

THE heterogeneous recombination of nitrogen and oxygen atoms on thermal-protection-system surfaces contributes to the aerothermal heating of hypersonic vehicles traversing the Earth's atmosphere. Modeling surface-catalyzed recombination reactions is an important aspect of computational fluid dynamics (CFD) predictions of aerothermal heating.

Most CFD heating computations neglect the possibility of nitric oxide formation via O + N surface reactions and treat oxygen and nitrogen recombination as two independent processes, $O + O \rightarrow O_2$ and $N + N \rightarrow N_2$, which operate in parallel. However, there is increasing evidence that surface-catalyzed NO formation is a significant pathway that should be included in such computations. For example, the inclusion of NO surface formation in a finite-rate surface chemistry model by Kurotaki [1] improved the agreement between measured flight data and aerothermal heating simulations. On the experimental side, Laux et al. [2] have used single-photon laser-induced fluorescence (LIF) to detect and compare relative NO number densities in front of different materials tested in a plasma wind tunnel. Copeland et al. [3] and, more recently, Pejaković et al. [4] performed experiments in a diffusion-tube sidearm reactor using two-photon LIF to monitor O-atom and N-atom number densities, inferring the O + N surface reaction from changes in the LIF signals as the O/N atomic ratio at the sidearm entrance was varied.

In the diffusion-tube sidearm reactor technique, atomic nitrogen is generated in a main flow tube using a microwave discharge and atomic oxygen is produced downstream via the rapid gas-phase titration reaction,

$$N + NO \rightarrow O + N_2 \tag{1}$$

which has a room-temperature rate coefficient of 2.7×10^{11} cm^3 molecule^{-1} s^{-1} [5]. As the resulting O/N/N_2 mixture flows past the

Received 14 September 2009; revision received 15 February 2010; accepted for publication 8 March 2010.

*Research Physicist, Molecular Physics Laboratory; dusan.pejakovic@sri.com.

†Senior Research Scientist, Molecular Physics Laboratory; jochen.marschall@sri.com. Senior Member AIAA.

‡Graduate Student, Mechanical and Aerospace Engineering Department; lduan@Princeton.edu.

§Assistant Professor, Mechanical and Aerospace Engineering Department; currently at University of Maryland, Department of Aerospace Engineering, College Park, Maryland 20742; mpmartin@umd.edu. Senior Member AIAA.

sidearm entrance, atomic species diffuse into the sidearm tube where they are lost by surface-catalytic reactions and, to a much lesser extent (because of the low pressures used in the experiment), gas-phase reactions. Under steady-state conditions, decaying atom number density profiles are established along the length of the sidearm tube. The experiments of Copeland et al. [3] demonstrated that, as O atoms were introduced in the N/N_2 mixture, the loss of N atoms from the gas-phase within the diffusion tube increased (i.e., the N-atom density dropped more quickly with distance into the tube). This accelerated N-atom loss was interpreted as resulting from the gas-phase reaction (1), where the source of NO was local $N + O$ surface recombination on the sidearm tube walls. They also predicted, but did not confirm experimentally, that the loss of O atoms from the gas phase should decrease with the addition of N atoms, given that each reaction event [Eq. (1)] regenerates a gas-phase O atom.

We have recently strengthened the experimental evidence provided by Copeland et al. [3] by adding sequential N- and O-atom LIF diagnostics and simultaneous concentration measurements at four different sidearm locations [4]. These measurements reproduced the findings of Copeland et al. [3] and confirmed their prediction of decreased O-atom loss in O/N mixtures. In addition, we developed a multispecies reaction-diffusion model for the diffusion-tube reactor that takes into account NO formation as a species boundary condition [4]. Simulations of the experimental conditions using this model reproduced the salient experimental results and imply that NO surface production is of comparable magnitude to the $O + O$ and $N + N$ surface recombination pathways on quartz surfaces at room temperature.

The logical progression in these studies is to confirm that the surface NO formation mechanism remains relevant at higher temperatures. In principle, the experimental approach used to infer the production of NO on quartz surfaces at room temperature could be extended to elevated temperatures. However two-photon LIF characterization of N- and O-atom number density profiles becomes significantly more complicated at higher temperatures. The primary difficulty is the rapidly increasing intensity of the blackbody radiation with increasing temperature, which creates a massive signal background in the 745 and 845 nm observation windows used to detect N and O atoms. In addition, atom number densities in the diffusion tube decrease with increasing temperature (in accordance with the ideal gas law at constant pressure), and the heterogeneous loss of atoms on quartz and silica surfaces also increases with temperature [6–10]. Moreover, the LIF scheme for O atoms probes only the population of atoms in the $J = 2$ level of the ground state, which also decreases with rising temperature [11,12]. Thus, extracting small LIF signals from the overwhelming thermal radiation background at high temperatures becomes extremely challenging.

We have developed a new experimental method for the investigation of NO surface production at elevated temperatures based on the direct detection of NO by single-photon LIF combined with photon counting signal detection. Surface-produced NO molecules are rapidly lost in the gas phase by reaction (1), thus steady-state NO number densities resulting from the balance between surface production and gas-phase reaction loss are expected to be quite small. However, surface-produced NO is still within the reach of sensitive single-photon LIF detection. Nitric oxide fluorescence is observed in the ultraviolet (UV) spectral region, hence the thermal radiation background is much smaller than in the near-infrared. With the use of isotopically labeled titration gases $^{15}N^{16}O$ and $^{15}N^{18}O$ single-photon LIF can unambiguously identify nitric oxide produced by the $O + N$ surface reaction.

This paper describes the results of measurements performed from room temperature up to 1200 K by this new experimental approach. The absolute number densities of surface-produced NO and the observed variations of NO number density with temperature and varying O/N ratios at the sidearm entrance are compared with predictions of the simple reaction-diffusion model developed in our previous work [4].

II. Experiment

A. Experimental Setup

The layout of our experiment is shown in Fig. 1. A partially dissociated nitrogen flow is produced by metering N_2 gas through a 100 W microwave discharge using a 100-sccm electronic mass flow controller. The main tube is made of glass and the sidearm tube is made of GE214 quartz. The partially dissociated gas flows down the main arm, past the opening of the dead-end sidearm tube, and into a scroll pump vacuum system. Gas pressures are measured near the opening and near the end of the sidearm tube using a Baratron capacitance manometer.

The sidearm tube is 147 cm long and has an inner diameter of 2.2 cm. Beginning 17 cm from the sidearm entrance, a 102 cm length of the sidearm tube is enclosed in a Carbolite four-section tube furnace capable of reaching 1373 K (1100°C.) The agreement between the quartz tube wall temperature and the furnace controller temperature readout was confirmed using an Omega type-*K* thermocouple probe in contact with the tube wall. The gas temperature was confirmed to be consistent with the furnace temperature using NO spectroscopic thermometry; the relative line intensities in the measured rotationally resolved $^{14}N^{16}O$ LIF spectra were consistent with those expected from theory, if the gas temperature in theoretically computed spectra was set equal to the furnace temperature (see below).

The excitation of NO molecules in the $A \leftarrow X(0,0)$ band is induced by UV light near 226 nm. A Lambda Physik XeCl excimer laser is used to pump a dye laser, and the resulting tunable output near 452 nm is frequency-doubled using a type-*B* beta barium borate crystal to produce UV radiation near 226 nm. The UV beam is directed down the centerline of the sidearm tube using a combination of dichroic mirrors and quartz prisms. A Pellin–Broca prism is used to separate visible from UV light and a Coherent Wavemaster wavemeter monitors the wavelength of the visible output exiting the prism. A quartz flat is used to direct a small fraction of the UV beam into a Molectron pyroelectric energy meter to monitor the stability of the laser pulse energy. To avoid saturation effects that would cause nonlinearities of the measured NO LIF signal with respect to the excitation energy, the UV excitation beam is attenuated by a factor of ~25 using UG-5 Schott colored glass filters. The UV excitation energy per laser pulse without attenuation is $\sim 0.2 - 0.3$ mJ.

The NO fluorescence is detected near 248 nm in the $A \rightarrow X(0,2)$ band using two Hamamatsu R928 photomultiplier tubes (PMTs) fit with 248 nm interference filters. The filters have full-width-at-half-maximum (FWHM) bandwidth of 10 nm. The two PMTs are mounted at different distances along the sidearm tube and view the NO fluorescence at right angles to the sidearm tube through 1 cm diameter quartz tubes extending through the furnace wall. For all the experiments reported here, the two PMTs were positioned 29 cm and 100 cm from the sidearm entrance. Two Stanford Research Systems (SRS) SR400 photon counters are used to record the PMT outputs allowing data collection at fluorescence signal levels lower than 1 photon per laser pulse. The typical counting period was 15 s, with a 0.5–1.5 μs gate width. The signal acquisition is synchronized with laser firing at a frequency of 10 Hz using a SRS DG535 digital delay generator. Instrument control and data collection are performed by a personal computer using LabView software.

The number density of O atoms in the gas is controlled by adding pure NO to the partially dissociated nitrogen flow upstream of the sidearm opening, using a Sierra Instruments Micro-Trak 100 flow controller with a resolution of 0.01 sccm. At the $N + NO$ titration endpoint, all N atoms are consumed and excess NO appears in the gas phase. The titration endpoint is determined by detecting the LIF signal of this excess NO titration gas.

The N_2 gas was acquired from Matheson Tri-Gas and had 99.999% purity, with an O_2 content less than 1 ppm. In control experiments (see below), a special N_2 gas grade with specified O_2 impurity less than 0.01 ppm was also used. The atomic purities of the isotopically labeled NO gases were (99% N, 98% O) for $^{15}N^{18}O$ and greater than 98% N for $^{15}N^{16}O$.

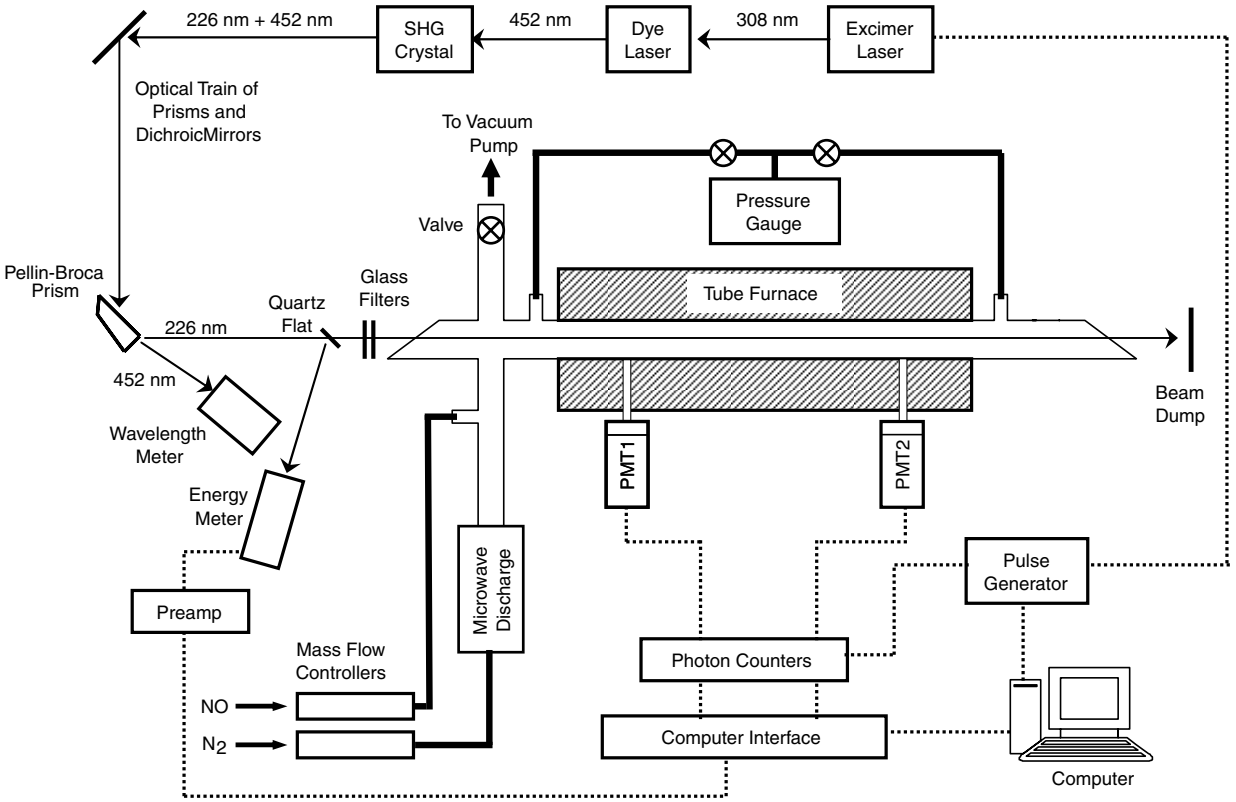

Fig. 1 Schematic of the experimental setup. SHG denotes second harmonic generation.

B. Measurement Procedure

The main difficulty encountered using this approach was to discriminate between the desired signal—that of the surface-produced NO—and background signals from NO present in the system from other sources. This problem was addressed by employing isotopically enriched titration gases as described below and illustrated in Fig. 2.

The first complication arises from the fact that, in the case of titration by $^{14}N^{16}O$, the titration agent is the same species as the one whose surface production is investigated (Fig. 2a). This raises the possibility that NO LIF signals detected in the sidearm reactor originate from titration gas not completely consumed in the titration region by reaction with N atoms. Additionally, the titration endpoint is never particularly sharp, in part due to instabilities in the gas flows, implying that, below but near the titration endpoint, the surface-produced NO signal could be superposed with the emerging signal from the NO titration gas. This makes it impossible to discern the behavior of the surface-produced NO signal near the endpoint.

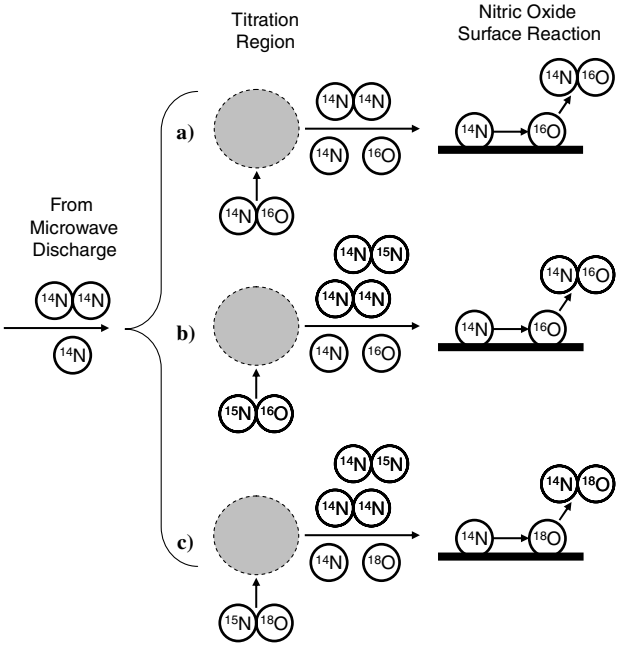

Fig. 2 Isotope labeling schemes for titration gas.

To bypass this problem, NO titration gas labeled by the ^{15}N isotope was used (see Fig. 2b). The main flow of nitrogen gas passing through the discharge produces ^{14}N atoms and the ^{15}N atoms from the ^{15}NO titration gas are incorporated into $^{15}N^{14}N$ molecules during the titration reaction. Any residual titration gas in the system would be ^{15}NO, whereas the surface-produced nitric oxide molecules are ^{14}NO. The measured rotationally resolved LIF excitation spectra of ^{15}NO and ^{14}NO are different and it is easy to trace the evolution of LIF signals of both species with the changes in the flow rate of the titration gas. The natural ratio $^{14}N/^{15}N$ is about 270, thus strictly speaking some ^{15}N is generated in the discharge and some ^{15}NO is produced on the surface, but at levels that are more than 2 orders of magnitude smaller than those of surface-produced ^{14}NO.

Gas-phase isotopic exchange reactions between N atoms and N_2 or NO molecules would complicate the interpretation of these experiments. However, the rate coefficients for these exchange reactions are extremely small. Back and Mui [13] have determined the upper limit for the rate coefficient of the exchange reaction $^{14}N + {}^{15}NO \rightarrow {}^{15}N + {}^{14}NO$ to be at least 250 times lower than that of reaction (1), based on experiments at both room temperature and 653 K (380°C). This implies that insignificant amounts of ^{15}N will be generated in the titration region and that the nitrogen isotope introduced in the NO titration gas will end up in a nitrogen molecule.

Back and Mui [13] have also determined an upper limit of 6.6×10^{-16} cm^3 molecule^{-1} s^{-1} for the rate coefficient of the exchange reaction $^{14}N + {}^{15}N^{15}N \rightarrow {}^{15}N + {}^{14}N^{15}N$ at a temperature of 1273 K (1000 °C). This rate coefficient is expected to decrease with decreasing temperature [14,15]. The reaction of concern for our experiments is $^{14}N + {}^{14}N^{15}N \rightarrow {}^{15}N + {}^{14}N^{14}N$. The interaction potentials for all isotopic permutations of the nitrogen exchange

reaction should be very similar and the generation of ^{15}N is statistically more probable from $^{15}N^{15}N$ than $^{14}N^{15}N$. Therefore, the reaction rate coefficient for $^{14}N + {}^{14}N^{15}N \rightarrow {}^{15}N + {}^{14}N^{14}N$ should be no higher than the limiting value determined by Back and Mui [13] for $^{14}N + {}^{15}N^{15}N \rightarrow {}^{15}N + {}^{14}N^{15}N$. Because of this low reaction rate coefficient, the $N + N_2$ exchange reaction is always much slower than reaction (1) in our experiments. For example, even for an N_2 to NO ratio of 500 (higher than any used in the experiments), reaction (1) is more than 80 times faster than the exchange reaction, assuming that the latter reaction has a rate coefficient equal to upper limit reported by Back and Mui [13].

A second, somewhat perplexing, complication arose because of a background $^{14}N^{16}O$ LIF signal observed at elevated temperatures, even without any titration gas added into the system, indicating that a source of oxygen atoms other than the NO titration agent was present in the system. This background signal was only observed with the microwave discharge running and was found to increase as the furnace temperature rose. We considered the possibility of residual O atoms adsorbed to the quartz surface and performed a test in which the background signal was monitored over a long time period (more than 3 h) with the N-atom flow present. A decreasing background signal is expected as the $N + O$ surface reaction depletes a finite supply of adsorbed O atoms. No such decrease was observed indicating that adsorbed O atoms are not a significant source of this background. Other immediate suspects were an O_2 impurity in the N_2 gas or an air leak into the system, both of which could lead to the production of O atoms in the discharge. The standard N_2 gas (less than 1 ppm specified O_2 impurity) was replaced by a special N_2 grade with specified O_2 impurity of less than 0.01 ppm, but the background NO signal remained unchanged, demonstrating that O_2 impurity in the N_2 gas was not the source. Using a He leak detector no leak was found in the system, however, the base pressure of the evacuated system once isolated from the pump did slowly rise either from outgassing of the system walls or from some undiscovered leak.

In a separate experiment, small amounts of air were added at the titration inlet at flow rates [$\sim$0.2 sccm (standard cubic centimeter per minute)] that produced pressure rises similar to the observed pressure rises in the isolated evacuated system. These air additions increased the NO background signal by factors of two to four, showing that the oxygen impurity does not need to be introduced upstream of the discharge to act as a source of O atoms. It is possible, although it seems unlikely, that some O_2 can diffuse against the bulk flow to dissociate in the discharge. Another possibility is that O atoms are created by gas-phase reactions of O_2 with electronically excited nitrogen molecules, particularly $N_2(A)$ and $N_2(B)$, created by the discharge or by $N + N$ gas-phase recombination in the post-discharge region [16,17].

To bypass the problem of the persistent $^{14}N^{16}O$ background signal, the isotopic labeling approach had to be used again, this time labeling both atoms of the NO titration gas by the ^{18}O and ^{15}N isotopes. This situation is illustrated in Fig. 2c. The titration reaction is now $^{14}N + {}^{15}N^{18}O \rightarrow {}^{18}O + {}^{14}N^{15}N$, and the possible surface reactions involving ^{14}N atoms generated in the discharge and ^{18}O atoms originating from the titration gas now become $^{14}N + {}^{18}O(s) \rightarrow {}^{14}N^{18}O$, $^{14}N(s) + {}^{18}O \rightarrow {}^{14}N^{18}O$, and $^{14}N(s) + {}^{18}O(s) \rightarrow {}^{14}N^{18}O$. Therefore, it is assured that the detected $^{14}N^{18}O$ molecules incorporate an O atom that is provided by the titration gas and an N atom that is not provided by the titration gas. The natural $^{16}O/^{18}O$ ratio is about 500; therefore, any contribution of ^{18}O coming from a residual air leak or outgassing to the $^{14}N^{18}O$ LIF signal is negligible.

The measurement protocol was as follows. Upon heating the furnace to a target temperature, the LIF excitation spectrum was first measured with discharge running at full power and without added NO titration agent. The spectrum was collected by slowly scanning the dye laser wavelength while counting photons in both PMT channels for a number (10–50) of laser pulses. The counting period was selected such that it did not diminish the wavelength resolution of the spectrum. For all elevated temperatures, the spectrum showed features of $^{14}N^{16}O$, which constitute the background signal discussed in the text above.

One of the isotopically labeled NO titration gases was then introduced and the spectrum was remeasured at different titration flow rates. The titration flow rate was increased in small increments until the endpoint was passed, as indicated by the disappearance of the surface-produced NO signal and the appearance of the LIF signal from the NO titration species.

Finally, the calibration procedure was performed: the discharge was turned off, $^{14}N^{16}O$ flown from a 10% NO balance N_2 cylinder was introduced in the system, and the LIF spectrum was measured. The calibration has two roles. First, it serves to cross-calibrate the two PMTs, which have different sensitivity factors. Those factors can be determined by comparing the PMT signals when both of them detect fluorescence from the same NO number density. Second, the LIF signal from a known $^{14}N^{16}O$ number density is used to extract the absolute number density of the surface-produced $^{14}N^{16}O$ by direct comparison of the LIF signal intensities. The $^{14}N^{16}O$ flow rate was set such that the LIF signal was similar in magnitude to the signal of surface-produced $^{14}N^{16}O$. This assured that the same part of the dynamic range of the detection system was used, such that the calibration procedure was insensitive to any nonlinearities in this system.

Ideally, $^{14}N^{18}O$ would be used for calibration, since this is the species produced by surface reaction in the experiments with the $^{15}N^{18}O$ titration gas. Unfortunately $^{14}N^{18}O$ was not commercially available during the time frame of this study. Therefore, experiments with $^{15}N^{18}O$ titration gas were used to determine the general trends of the (unambiguously) surface-produced $^{14}N^{18}O$ number density as a function of titration gas flow rate. Absolute values of the surface-produced NO number density at different elevated temperatures were determined separately from $^{15}N^{16}O$ titration experiments that generated $^{14}N^{16}O$. The LIF signals collected during these experiments were corrected by subtracting the background $^{14}N^{16}O$ signals (discussed previously) and then comparing the signal intensity to that in calibration measurements performed using $^{14}N^{16}O$.

III. Experimental Results

For all the experiments reported here, the input N_2 flow was 73 sccm, the titration endpoint corresponded to a $\sim$0.6 sccm NO flow, and the total pressure in the diffusion tube was 58.5 Pa.

To minimize the data acquisition time, the dye laser wavelength was scanned over relatively narrow spectral regions that contain several well-separated lines of each of the NO isotopic species of interest. Figure 3 shows spectra collected in the experiments at 1000 K using $^{15}N^{16}O$ as the titration agent. The experimental spectra were measured at a distance of 100 cm down the diffusion tube and represent the sum photon count for 40 laser pulses. Below the endpoint (observed at a $^{15}N^{16}O$ flow rate of 0.57 sccm), the spectrum shows practically only $^{14}N^{16}O$ features; the very weak $^{15}N^{16}O$ features in the 226.30–226.32 nm range may be due to residual $^{15}N^{16}O$ left over in the diffusion tube from the previous run above the endpoint and partly due to $^{15}N^{16}O$ naturally present in the $^{14}N^{16}O$ cylinder. The spectrum shows raw photon count, and the noise level in the spectrum illustrates the size of the background blackbody radiation signal relative to the LIF signal. Above the endpoint, only strong $^{15}N^{16}O$ features are observed (bottom spectrum in Fig. 3).

Figure 3 also shows a theoretical rotationally resolved $^{14}N^{16}O$ LIF excitation spectrum, obtained using the LIFBASE spectral simulation software [18]. The simulation used Gaussian line profiles with a fixed linewidth of 0.02 Å (FWHM), approximately equal to that in the experimental spectrum. The temperature in the simulation was then adjusted in steps of 25 K until the relative line intensities (peak heights) for $\sim$10 lines in the simulation (top plot in Fig. 3) were nearly identical to experimental spectrum (the middle plot in Fig. 3.) The best agreement was found for a simulated gas temperature of 1000 K, consistent with the measured furnace temperature.

For either NO species, there are several lines that are well separated from the lines of the other species and that can be used unambiguously for species identification. After normalizing the spectrum by dividing the signal with the measured laser pulse energy, four well-separated $^{14}N^{16}O$ lines were fitted with Gaussians and the

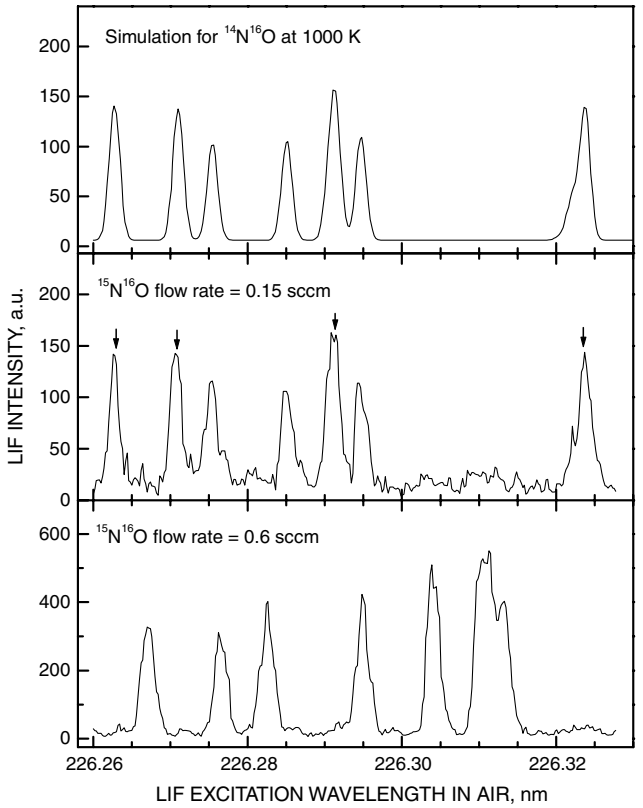

Fig. 3 Simulated spectrum (top) and experimental LIF excitation spectrum, with a $^{15}N^{16}O$ titration flow below the titration endpoint, showing lines of $^{14}N^{16}O$ (middle). The lines used to calculate changes of LIF intensities with the titration flow rate (Fig. 4) are labeled by arrows. Experimental LIF spectrum, with a $^{15}N^{16}O$ titration flow above the titration endpoint, showing lines of $^{15}N^{16}O$ (bottom). Arbitrary units are denoted by a.u.

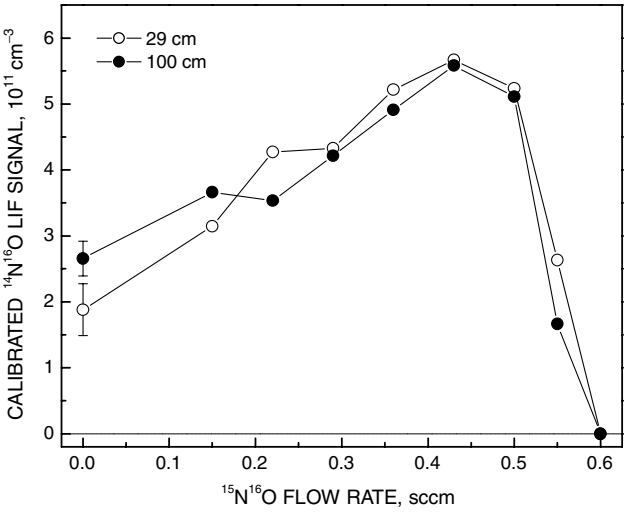

Fig. 4 LIF signal intensity for $^{14}N^{16}O$ as a function of the $^{15}N^{16}O$ titration flow rate at 1200 K. The plotted values represent integrated photon counts for several selected lines, as indicated in Fig. 3. The error bars are estimated uncertainties, and they are shown for only one data point in each curve, for clarity.

summed area of the four Gaussians was used to trace the dependence of the $^{14}N^{16}O$ LIF signal on the titration gas flow rate. This dependence is shown in Fig. 4, in which absolutely calibrated signals for both PMTs are plotted. The number density values obtained by $^{14}N^{16}O$ calibration are in the 10^{11} cm^{-3} range. Starting from a nonzero value at zero $^{15}N^{16}O$ flow, the $^{14}N^{16}O$ number density increases up to about 0.45 sccm and then rapidly falls towards zero as the flow rate approaches the endpoint value.

The background NO LIF signal is sizable; its value when no titration gas is added is about half of the total signal peak value reached near 0.45 sccm (Fig. 4). The behavior of the background $^{14}N^{16}O$ as a function of the titration flow rate has to be understood before it can be subtracted from the total signal and this was made possible by the $^{15}N^{18}O$ titration experiments.

Figure 5 shows spectra measured at 1200 K using $^{15}N^{18}O$ titration. The spectra were measured at a distance of 100 cm down the diffusion tube, and each data point represents the sum photon count for 20 laser pulses. A different spectral region was selected than in the case of $^{15}N^{16}O$ titration. The situation is also more complicated in this case, because both $^{14}N^{16}O$ and $^{14}N^{18}O$ features are observed in the spectrum for all titration flow rates below the endpoint. However, $^{14}N^{16}O$ and $^{15}N^{18}O$ spectra that were measured separately, using pure $^{14}N^{16}O$ and $^{15}N^{18}O$ flowed from the respective cylinders, allows unambiguous assignment of the observed $^{14}N^{16}O$ transitions and, by exclusion, those transitions that belong to neither $^{14}N^{16}O$ nor $^{15}N^{18}O$ are assigned to $^{14}N^{18}O$. The line assignments, as well as the lines used to trace the dependences of $^{14}N^{16}O$ and $^{14}N^{18}O$ number densities on the titration flow rate are marked in Fig. 5. The bottom panel in Fig. 5 shows the spectrum measured above the endpoint, showing only the strong lines of the $^{15}N^{18}O$ titration agent.

Figure 6 shows the dependences of the $^{14}N^{16}O$ and $^{14}N^{18}O$ number densities on the $^{15}N^{18}O$ titration flow rate. The signals from the two

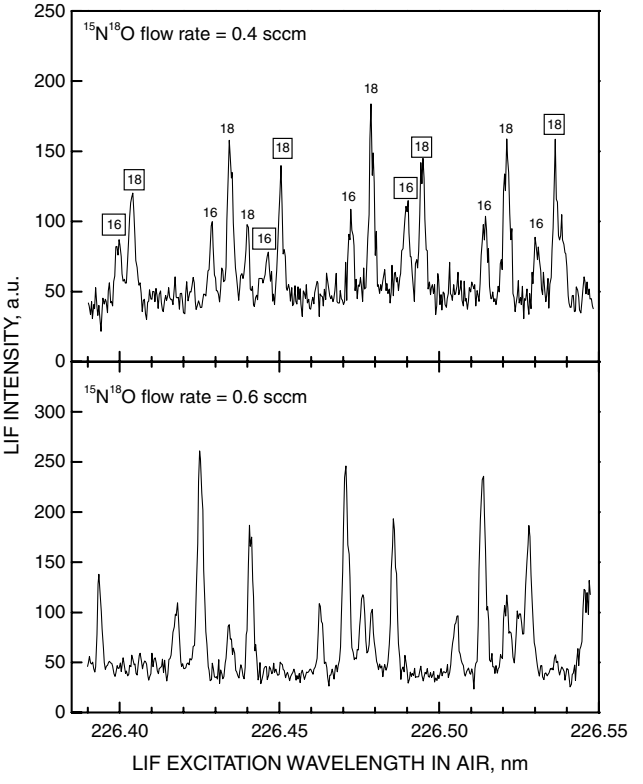

Fig. 5 LIF spectra at 1200 K obtained using $^{15}N^{18}O$ titration. The spectrum measured below the titration endpoint (top), showing lines of $^{14}N^{16}O$ (labeled by 18) and $^{14}N^{18}O$ (labeled by 16). The lines that were used to calculate the changes of LIF intensities with the titration flow rate (Fig. 6) have labels enclosed in squares. The spectrum measured above the titration endpoint, showing only $^{15}N^{18}O$ lines (bottom).

PMTs have been cross calibrated, as described above. The $^{14}N^{16}O$ background signal decreases with the flow rate in an approximately linear fashion, and a linear fit to this dependence would yield a nonzero value at the titration endpoint. Near the endpoint, the $^{14}N^{16}O$ signal drops to zero rather abruptly. The decrease in the background $^{14}N^{16}O$ signal with increasing titration flow is not surprising, given that no new ^{16}O atoms are added in the system, whereas the number

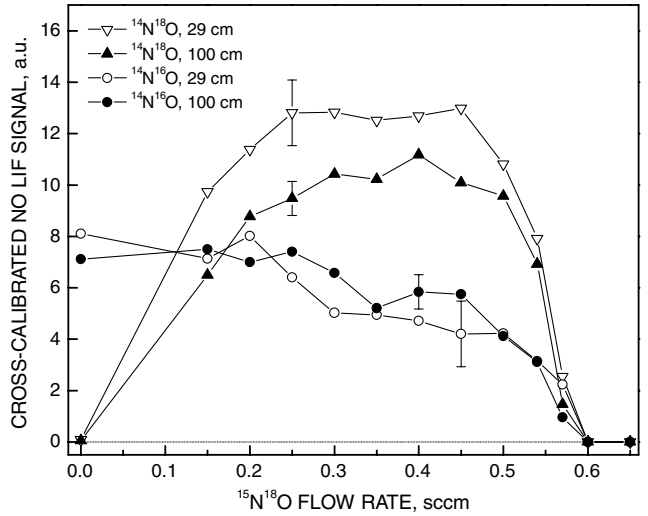

Fig. 6 LIF signal intensities for $^{14}N^{18}O$ and $^{14}N^{16}O$ as functions of the $^{15}N^{18}O$ titration flow rate at 1200 K. The plotted values represent integrated photon counts for several selected lines, as indicated in Fig. 5. The estimated uncertainties (indicated by the error bars) are shown for only one data point in each curve, for clarity.

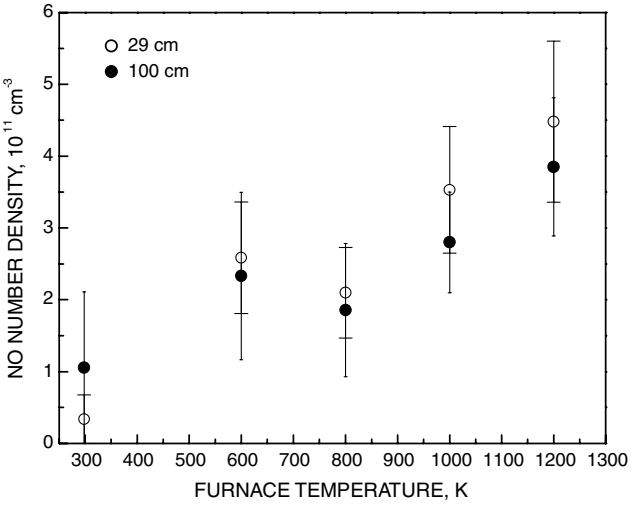

Fig. 7 Number density of surface-produced $^{14}N^{16}O$ as a function of temperature for two positions down the diffusion tube. The data were obtained using $^{15}N^{16}O$ titration, with a titration flow rate corresponding to 70% of the endpoint. The background signal was subtracted to obtain the $^{14}N^{16}O$ density due solely to the O atoms introduced by titration (see text).

density of ^{14}N atoms decreases with the addition of $^{15}N^{18}O$ titration flow. The strong deviation from linear dependence near the endpoint and the abrupt drop to zero are harder to understand without a detailed model. However, it is noted that the probed steady-state $^{14}N^{16}O$ number density is a result of a competition between the surface-catalyzed production and gas-phase removal by reaction with N atoms; rates for both processes increase with the N-atom number density and, in such a situation, strong nonlinearities near zero N-atom number density (endpoint) are not surprising.

The $^{14}N^{18}O$ signal plotted in Fig. 6 is zero at zero titration flow, and it increases with flow rate with a noticeable curvature. Similar to the data in Fig. 4, the curve exhibits a rather broad peak near 2/3 of the endpoint flow rate and then rather abruptly decreases to zero. The $^{14}N^{16}O$ data in Fig. 4, which include the flow rate-dependent background signal contribution, show no significant curvature below 0.4 sccm, but the experimental uncertainty (indicated by the error bars in Figs. 4 and 6) is significant enough that such curvature cannot be excluded. The fact that the $^{14}N^{18}O$ signal is purely titration-induced (i.e., it disappears at both zero titration flow and titration endpoint) unambiguously proves that $^{14}N^{18}O$ is a result of a reaction between ^{18}O atoms introduced by titration and ^{14}N atoms produced by N_2 dissociation in the discharge. The general shape of the $^{14}N^{18}O$ signal dependences plotted in Fig. 6 provides a key test for the surface chemistry model, as detailed below.

For the purpose of analysis, it is assumed that the total NO number density is a simple sum of the background and titration-induced number densities for any titration flow rate. The titration-induced number density is then extracted using $^{15}N^{18}O$ titration data as guidance. At zero titration flow, all of the NO number density plotted in Fig. 4 is a result of the background production. At, e.g., 0.4 sccm titration flow rate, Fig. 6 indicates that this initial background number density is reduced by about 50% at a distance of 29 cm down the tube. Thus, from the total NO signal at 0.4 sccm, 50% of the initial (zero-flow) signal is subtracted to obtain the titration-induced number density. Such analysis was done for all investigated temperatures and the results are plotted in Fig. 7. The room-temperature NO signals were barely distinguishable from noise, hence the 2σ error bars in Fig. 7 include zero. The NO density exhibits a relatively rapid increase with temperature, except for the possible drop between 600 and 800 K.

Figures 6 and 7 provide experimental proof for the surface formation of NO on quartz and show how the number density of surface-produced NO varies with temperature, titration condition and location along the side arm. In the next two sections, details are presented of a simple numerical reaction-diffusion model of the sidearm reactor that includes NO surface formation as a boundary condition. The model predictions for the NO number density in the side arm are compared with the experiment.

IV. Modeling

A. Model Formulation and Solution

The reaction-diffusion model applied to interpret the experimental results was described in detail and its computational performance verified in our previous paper [4]. Therefore, only a cursory description is given here.

The sidearm reactor is modeled as a tube of length $L = 147$ cm and a uniform radius $R = 1.1$ cm, closed at one end by a disk normal to the tube axis. Concentration profiles are obtained by the simultaneous solution of eight species continuity equations of the form:

$$\frac{\partial \rho_s}{\partial t} + \frac{1}{r}\frac{\partial}{\partial r}(r j_{sr}) + \frac{\partial}{\partial z}(j_{sz}) = w_s \tag{2}$$

for $s = $ N, O, N_2, O_2, NO, N_2O, NO_2, and O_3. In Eq. (2), ρ_s is the species mass density, w_s represents the rate of species production due to gas-phase chemical reactions, and j_{sr} and j_{sz} are the diffusive mass fluxes in the radial and axial directions relative to the mass average velocity of the mixture. The diffusive mass fluxes in the radial and axial directions are related to the corresponding diffusion velocities by $j_{sr} = \rho_s \upsilon_{sr}$ and $j_{sz} = \rho_s \upsilon_{sz}$. The ideal gas law is used as the equation of state. The reactor is isobaric and the gas temperature is assumed equal to the local wall temperature (which is specified), thus solutions of the momentum and energy equations are not required to obtain concentration profiles. The species mass flux vector is given by

$$\mathbf{j}_s = -(cM_sD_s)\nabla x_s + \frac{\rho_s}{\rho}\sum_r (cM_rD_r)\nabla x_r \tag{3}$$

with M_s as the species molar mass, x_s as the species mole fraction, and D_s as the effective binary diffusion coefficient for species s in the gas mixture; c and ρ are the total molar and mass densities of the gas, respectively. Effective diffusion coefficients in the multicomponent gas mixtures of the experiment are computed using the friction-weighted self-consistent effective binary diffusion approximation [19,20] with the weighing factor set equal to the mole fraction for each species. The required binary diffusion coefficients for all species pairs were computed using collision integrals compiled by

Table 1 Gas-phase reactions used in the computational model

	Reaction	Rate coefficient [a]	References
R1	$N + NO \rightarrow N_2 + O$	$k_1 = 2.7 \times 10^{-11} T^0 \exp(0/T)$	[5]
R2	$O + O_2 + M \rightarrow O_3 + M$	$k_2 = 5.29 \times 10^{-28} T^{-2.4} \exp(0/T)$	[24]
R2b	$O_3 + M \rightarrow O + O_2 + M$	$k_{2b} = 4.13 \times 10^{-10} T^0 \exp(-11430/T)$	[25]
R3	$O + O_3 \rightarrow O_2 + O_2$	$k_3 = 8.6 \times 10^{-12} T^0 \exp(-2090/T)$	[25]
R4	$O + N + M \rightarrow NO + M$	$k_4 = 1.8 \times 10^{-31} T^{-0.5} \exp(0/T)$	[5]
R5	$O + NO + M \rightarrow NO_2 + M$	$k_5 = 4.2 \times 10^{-33} T^0 \exp(940/T)$	[5]
R6	$O + NO_2 \rightarrow NO + O_2$	$k_6 = 1.7 \times 10^{-11} T^0 \exp(-300/T)$	[5]
R7	$N + N + M \rightarrow N_2 + M$	$k_7 = 8.3 \times 10^{-34} T^0 \exp(500/T)$	[5]
R8	$O + O + M \rightarrow O_2 + M$	$k_8 = 1.57 \times 10^{-34} T^0 \exp(900/T)$	[25]
R9	$N + NO_2 \rightarrow N_2O + O$	$k_9 = 5.8 \times 10^{-12} T^0 \exp(220/T)$	[24]

[a]Bimolecular rate coefficients are in the units of cm^3 $molecule^{-1}$ s^{-1}. Termolecular rate coefficients are in the units of cm^6 $molecule^{-2}$ s^{-1}, and the collision partner M is taken as N_2.

Wright et al., [21,22] implemented using the curve fit formulas of Gupta et al. [23] Collision integrals for ozone were unavailable and were approximated by those given for carbon dioxide. Diffusion coefficients and reaction rate coefficients (see below) are taken as independent of species isotopic composition.

Table 1 lists reaction rate coefficient expressions for the 10 gas-phase reactions involving dissociated oxygen and nitrogen species included in the model. The rate coefficients are expressed as $k = AT^n \exp[-(E/\Re)/T]$, with the constants A, n, and $E/\Re$ taken from various literature sources (some constants are zero). Because ozone thermally dissociates at appreciable rates above ~500 K, the reverse reaction for R2 (R2b) is included; all other reverse reaction rate coefficients are set to zero.

Species production by surface-catalyzed reactions must be balanced by the species diffusive flux at the wall: $-j_{s,w} = w_{s,w}$. For reactant species, the production rates at the surface are expressed as their surface impingement rate ($\rho_{s,w}\bar{v}_s/4$) times a loss probability, γ_s, defined as the fraction of impinging reactant flux removed permanently from the gas phase. The loss probability represents the total efficiency of all operating surface reaction pathways that remove species s on a particular surface under a particular combination of temperature, pressure, and gas composition. When a reactant can form multiple products, branching fractions, $f_{s,r}$, are defined as the fraction of impinging reactant removed permanently from the gas phase that participates in forming product species r. The absolute lower and upper bounds on both γ_s and $f_{s,r}$ are 0 and 1, but this range may be reduced by the availability of partner reactants. For a partially dissociated mixture of oxygen and nitrogen with three available surface reaction pathways ($O + O \rightarrow O_2$, $N + N \rightarrow N_2$, and $O + N \rightarrow NO$), element conservation dictates the constraint:

$$(1 - f_{O,O_2})\gamma_O \rho_{O,w} \bar{v}_O / M_O = (1 - f_{N,N_2})\gamma_N \rho_{N,w} \bar{v}_N / M_N \quad (4)$$

In all the simulations that follow, the total pressure is 58.5 Pa, the input N_2 flow is 73 sccm and the titration endpoint is at 0.6 sccm added NO. A zero-flux boundary condition is applied along the tube centerline and the gas composition at the sidearm entrance is fixed based on a selected titration condition. Species boundary conditions on the sidearm surfaces are provided by specifying values for γ_O, γ_N, f_{O,O_2}, and f_{N,N_2}, with the branching fraction of the major reactant species superseded by element conservation.

B. Simulation Results

In our previous room-temperature experiments, reasonable agreement was found between measured and simulated O-atom and N-atom profiles along the sidearm tube by setting $\gamma_O = \gamma_N = 1 \times 10^{-5}$ and specifying $f_{O,O_2} = f_{N,N_2} = 0.5$ [4]. The loss probability of O and N atoms by surface recombination on quartz increases with temperature, although the reported magnitude and functional dependence of this effect varies greatly between researchers [6–10]. Here, the equality $\gamma_O = \gamma_N = \gamma$ is maintained and an exponential function, $\gamma = A[1 - \exp(-T/B)]$, is used to interpolate between 1×10^{-5} at 298 K (γ_{298}) and a specified value at 1200 K (γ_{1200}). This exponential function produces an initial rapid rise of loss probability with temperature followed by a gradual approach to a high-temperature plateau, a behavior which seems more in line with experimental observations than a simple linear dependence through this temperature range [6–10].

In the initial set of computations, the branching fractions were set at the same value as in the room-temperature case, $f_{O,O_2} = f_{N,N_2} = 0.5$, and the high-temperature loss probability was adjusted until the value of gas-phase NO number density was approximately equal to that determined experimentally at 1200 K for a titration gas flow of 0.4 sccm (or 2/3 of the endpoint). This is accomplished for a 1200 K loss probability of $\gamma_{1200} = 3 \times 10^{-4}$, a value consistent with published data [6–10].

The simulation results are shown in Figs. 8a and 8b. Figure 8a plots the predicted number density of surface-produced NO at a titration gas flow of 0.4 sccm as a function of furnace temperature and can be compared with Fig. 7. Figure 8b shows the predicted number density of surface-produced NO as a function of titration gas flow at a furnace temperature of 1200 K and can be compared with the $^{14}N^{18}O$ data plotted in Fig. 6.

Despite the many reaction and diffusion parameters that must be input into the program, as well as the simple description of surface chemistry employed, this reaction-diffusion model reproduces many important features of the experiment, including the approximate magnitude of the surface-produced NO concentration, its increase with surface temperature and its rise and fall with added titration gas flow. Computations made with or without reaction R4 over the entire range of experimental conditions produce essentially identical numerical results; therefore, the gas-phase production of NO is negligible compared with the surface production of NO.

Reaction R1 is obviously a key player in this model, given its large rate coefficient and the fact that it directly affects the steady-state density of surface-produced NO that persists in the gas phase. Room-

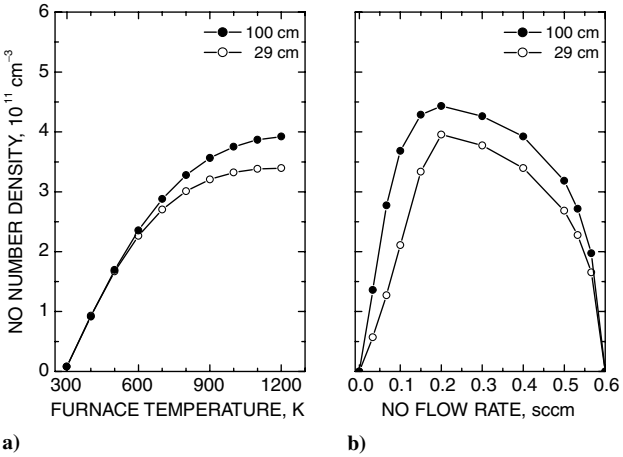

Fig. 8 The number density of surface-produced NO at distances of 29 and 100 cm from the sidearm opening as a) a function of furnace temperature for a titration gas flow of 0.4 sccm, and b) a function of titration gas flow at a furnace temperature of 1200 K.

temperature values of the R1 rate coefficient have been recommended based on extensive literature reviews by Baulch et al. [5] (2.7×10^{11} cm^3 molecule^{-1} s^{-1} with an uncertainty of $\pm 20\%$) and Sander et al. [24] (3.0×10^{11} cm^3 molecule^{-1} s^{-1} with an uncertainty of $\pm 30\%$.) Measurements made below room temperature indicate that the rate constant decreases as the temperature rises [24], while measurements at elevated temperatures above 1400 K indicate the opposite trend [26]. In the intermediate temperature range of our experiments, the rate coefficient reaches its minimum value, but reliable experimental rate coefficient measurements are lacking. Recent theoretical calculations [27] predict that the rate coefficient has a very shallow minimum near 550 K, only about 6% smaller than the room-temperature value. Baulch et al. [5] recommend retaining the room-temperature value with expanded error bars as temperature increases, and here we adopt this recommendation.

To test the sensitivity of the model to the R1 rate coefficient, the value recommended by Baulch et al. [5] was varied by about $\pm 20\%$ ($\pm 0.6 \times 10^{-11}$ cm^3 molecule^{-1} s^{-1}) and the process of adjusting the high-temperature loss probability γ_{1200} to match the 1200 K experimental NO number densities was repeated. This procedure produced high-temperature loss probabilities with relative changes similar to those of k_1 (i.e., $\gamma_{1200} = 2.3 \times 10^{-4}$ for $k_1 = 2.1 \times 10^{-11}$ cm^3 molecule^{-1} s^{-1} and $\gamma_{1200} = 3.7 \times 10^{-4}$ for $k_1 = 3.3 \times 10^{-11}$ cm^3 molecule^{-1} s^{-1}). Model simulations for each of these combinations produced identical results to those plotted in Fig. 8b. Given the uncertainties in the literature values of γ and k_1, any of these combinations is plausible and these two model inputs cannot be more tightly constrained by the present experiment.

There are two noteworthy qualitative differences between model predictions and experiment. First, the measured number densities of surface-produced NO are always higher at the 29 cm location than at the 100 cm location, whereas the model produces the opposite trend. Second, the experimental maximum of the number density of surface-produced NO occurs near 0.4 sccm of added titration gas, while the model produces a maximum near 0.2 sccm. The computed NO number density at 29 cm can be forced to exceed that at 100 cm by setting the high-temperature loss probability to 1×10^{-4} or less, but then the absolute value of the computed NO number density is more than a factor of 3 lower than was measured at 1200 K. The location of the NO maximum can be shifted to higher titration gas flows by changing the branching fractions to favor the surface recombination of O atoms to form O_2 ($f_{O,O_2} > 0.5$) and the surface reaction of N atoms to form NO ($f_{N,N_2} < 0.5$). Changes in the opposite direction will shift the computed maximum to lower titration gas flows, but this is the wrong direction for agreement with the experiment.

Given the simplicity of the surface reaction model used, which is only constrained by element conservation and does not incorporate finite-rate surface reactions, further manipulations of the ($\gamma_O, \gamma_N, f_{O,O_2}, f_{N,N_2}$) parameter space to reproduce finer experimental details seem unwarranted.

Although models of this type are often used for parametric studies seeking to bound catalytic effects [28], a more attractive approach for including the NO surface formation in CFD computations is with a finite-rate surface chemistry model as implemented by Kurotaki [1] and others [29–34] (i.e., a model that incorporates kinetic mechanisms like adsorption, thermal desorption, Eley–Rideal recombination, and Langmuir–Hinschelwood recombination). Unfortunately, these models contain large numbers of numerical parameters that must be chosen by theory and/or adjusted to reproduce experiments. More experimental data are required at higher temperatures and over a larger range of gas pressures and compositions, to enable the construction of a suitable finite-rate chemistry model for our experiments. Such measurements are currently underway in our laboratory.

V. Conclusions

The experimental and simulation results presented here confirm the importance of surface-catalyzed production of nitric oxide from the recombination of atomic oxygen and atomic nitrogen. The experiments unambiguously demonstrate that NO is produced via reactions on quartz surface from room temperature up to 1200 K. Computational simulations of the sidearm reactor performed using a simple multispecies reaction-diffusion model that incorporates surface production of NO and gas-phase reaction of NO and N atoms, qualitatively reproduce the experimental observations. The results imply that the surface production of NO is comparable in magnitude to the surface production of O_2 and N_2 over a broad temperature range of 300–1200 K.

Together with the CFD simulations of Kurotaki [1], which indicate the importance of NO surface formation in matching computational and measured heating data for the orbital-reentry-experiment flight and the LIF detection of NO over different material surfaces during plasma testing by Laux et al. [2], the present work strengthens the case for including O + N surface recombination in CFD simulations of hypersonic flight and plasma testing.

Acknowledgments

This work was supported jointly by the High Temperature and Aerospace Materials Program and the Hypersonics Program of the U.S. Air Force Office of Scientific Research, through the prime contract FA9556-05-1-10490.

References

[1] Kurotaki, T., "Catalytic Model on SiO_2-Based Surface and Application to Real Trajectory," *Journal of Spacecraft and Rockets*, Vol. 38, No. 5, 2001, pp. 798–800. doi:10.2514/2.3749

[2] Laux, T., Feigl, M., Stöckle, T., and Auweter-Kurtz, M., "Estimation of the Surface Catalyticity of PVD-Coatings by Simultaneous Heat Flux and LIF Measurements in High Enthalpy Air Flows," AIAA Paper 2000-2364, June 2000.

[3] Copeland, R. A., Pallix, J. B., and Stewart, D. A., "Surface-Catalyzed Production of NO from Recombination of N and O Atoms," *Journal of Thermophysics and Heat Transfer*, Vol. 12, No. 4, 1998, pp. 496–499. doi:10.2514/2.6395

[4] Pejaković, D., Marschall, J., Duan, L., and Martin, M. P., "Nitric Oxide Production from Surface Recombination of Oxygen and Nitrogen Atoms," *Journal of Thermophysics and Heat Transfer*, Vol. 22, No. 2, 2008, pp. 178–186. doi:10.2514/1.33073

[5] Baulch, D. L., Drysdale, D. D., and Horne, D. G., *Evaluated Kinetic Data for High Temperature Reactions, Volume 2: Homogeneous Gas Phase Reactions of the* $H_2 - N_2 - O_2$ *System*, Butterworths, London, 1973.

[6] Bedra, L., and Balat-Pichelin, M., "Comparative Modeling Study and Experimental Results of Atomic Oxygen Recombination on Silica-Based Surfaces at High-Temperature," *Aerospace Science and Technology*, Vol. 9, No. 4, 2005, pp. 318–328. doi:10.1016/j.ast.2005.01.011

[7] Bedra, L., Rutigliano, M., Balat-Pichelin, M., and Cacciatore, M., "Atomic Oxygen Recombination on Quartz at High Temperature: Experiments and Molecular Dynamics Simulation," *Langmuir*, Vol. 22, No. 17, 2006, pp. 7208–7216. doi:10.1021/la0600321

[8] Greaves, J. C., and Linnett, J. W., "Recombination of Atoms at Surfaces, Part 6: Recombination of Oxygen Atoms on Silica from 20°C to 600°C," *Transactions of the Faraday Society*, Vol. 55, 1959, pp. 1355–1361. doi:10.1039/tf9595501355

[9] Kaufman, F., "Reactions of Oxygen Atoms," *Progress in Reaction Kinetics*, edited by C. Porter, Vol. 1, Pergamon, Oxford, England, U.K., 1961, pp. 3–39.

[10] Marschall, J., Chamberlain, A., Crunkleton, D., and Rogers, B., "Catalytic Atom Recombination on ZrB_2/SiC and HfB_2/SiC Ultrahigh-Temperature Ceramic Composites," *Journal of Spacecraft and Rockets*, Vol. 41, No. 4, 2004, pp. 576–581. doi:10.2514/1.2879

[11] Bischel, W. K., Perry, B. E., and Crosley, D. R., "Detection of Fluorescence from O and N Atoms Induced by Two-Photon Absorption," *Applied Optics*, Vol. 21, No. 8, 1982, pp. 1419–1429. doi:10.1364/AO.21.001419

[12] Bischel, W. K., Perry, B. E., and Crosley, D. R., "Two-Photon Laser-Induced Fluorescence in Oxygen and Nitrogen Atoms," *Chemical Physics Letters*, Vol. 82, No. 1, 1981, pp. 85–88. doi:10.1016/0009-2614(81)85112-3

[13] Back, R. A., and Mui, J. Y. P., "The Reactions of Active Nitrogen with $N^{15}O$ and N_2^{15}," *Journal of Physical Chemistry*, Vol. 66, No. 7, 1962, pp. 1362–1364. doi:10.1021/j100813a506

[14] Wang, D., Stallcop, J. R., Huo, W. M., Dateo, C. E., Schwenke, D. W., and Partridge, H., "Quantal Study of the Exchange Reaction for $N + N_2$ Using an Ab Initio Potential Energy Surface," *Journal of Chemical Physics*, Vol. 118, No. 5, 2003, pp. 2186–2189. doi:10.1063/1.1534092

[15] Garcia, E., Saracibar, A., Laganà, A., and Skouteris, D., "The Shape of the Potential Energy Surface and the Thermal Rate Coefficients of the $N + N_2$ Reaction," *Journal of Physical Chemistry A*, Vol. 111, No. 41, 2007, pp. 10362–10368. doi:10.1021/jp072345a

[16] Gordiets, B. F., Ferreira, C. M., Guerra, V. L., Loureiro, J. M., Nahorny, J., Pagnon, D., and Vialle, M., "Kinetic Model of a Low-Pressure $N_2 - O_2$ Flowing Glow Discharge," *IEEE Transactions on Plasma Science*, Vol. 23, No. 4, 1995, pp. 750–768. doi:10.1109/27.467998

[17] Guerra, V., Sá, P. A., and Loureiro, J., "Role Played by the $N_2(A^3\Sigma_u^+)$ Metastable in Stationary N_2 and $N_2 - O_2$ Discharges," *Journal of Physics D: Applied Physics*, Vol. 34, No. 12, 2001, pp. 1745–1755. doi:10.1088/0022-3727/34/12/301

[18] Luque, J., and Crosley, D. R.,"LIFBASE: Database and Spectral Simulation for Diatomic Molecules," SRI International, MP-99-0099, Menlo Park, CA, 1999, http://www.sri.com/psd/lifbase/ [retrieved 29 June 2009].

[19] Ramshaw, J. D., "Self-Consistent Effective Binary Diffusion in Multicomponent Gas Mixtures," *Journal of Non-Equilibrium Thermodynamics*, Vol. 15, No. 3, 1990, pp. 295–300. doi:10.1515/jnet.1990.15.3.295

[20] Ramshaw, J. D., and Chang, C. H., "Friction-Weighted Self-Consistent Effective Binary Diffusion Approximation," *Journal of Non-Equilibrium Thermodynamics*, Vol. 21, No. 3, 1996, pp. 223–232. doi:10.1515/jnet.1996.21.3.223

[21] Wright, M. J., Bose, D., Palmer, G. E., and Levine, E., "Recommended Collision Integrals for Transport Property Computations, Part 1: Air Species," *AIAA Journal*, Vol. 43, No. 12, 2005, pp. 2558–2564. doi:10.2514/1.16713

[22] Wright, M. J., Hwang, H. H., and Schwenke, D. W., "Recommended Collision Integrals for Transport Property Computations Part 2: Mars and Venus Entries," *AIAA Journal*, Vol. 45, No. 1, 2007, pp. 281–288. doi:10.2514/1.24523

[23] Gupta, R., Yos, J., Thompson, R., and Lee, K., "A Review of Reaction Rates and Thermodynamic and Transport Properties for an 11-Species Air Model for Chemical and Thermal Nonequilibrium Calculations to 30,000 K," NASA, RP-1232, Aug. 1990.

[24] Sander, S. P., Friedl, R. R., Golden, D. M., Kurylo, M. J., Moortgat, G. K., Wine, P. H., Ravishankara, A. R., Kolb, C. E., Molina, M. J., Finlayson-Pitts, B. J., Huie, R. E., and Orkin, V. L., "Chemical Kinetics and Photochemical Data for Use in Atmospheric Studies: Evaluation Number 15," NASA, Jet Propulsion Laboratory Publ. 06-2, 10 July 2006.

[25] Baulch, D. L., Drysdale, D. D., Duxbury, J., and Grant, S. J., *Evaluated Kinetic Data for High Temperature Reactions, Volume 3. Homogeneous Gas Phase Reactions of the* $O_2 - O_3$ *System, the* $CO - O_2 - H_2$ *System, and of Sulfur-Containing Species*, Butterworths, London, 1976.

[26] Baulch, D. L., Cobos, C. J., Cox, R. A., Frank, P., Hayman, G., Just, T., Kerr, J. A., Murrells, T., Pilling, M. J., Troe, J., Walker, R. W., and Warnatz, J., "Evaluated Kinetic Data for Combustion Modelling. Supplement 1," *Journal of Physical and Chemical Reference Data*, Vol. 23, No. 6, 1994, pp. 847–1033. doi:10.1063/1.555953

[27] Gamallo, P., Sayós, R., González, M., Petrongolo, C., and Defazio, P., "Quantum Real Wave-Packet Dynamics of the $N(^4S) + NO(X^2P) \rightarrow N_2(X^1\Sigma_g^+) + O(^3P)$ Reaction on the Ground and First Excited Triplet Potential Energy Surfaces: Rate Constants, Cross Sections, and Product Distributions," *Journal of Chemical Physics*, Vol. 124, No. 17, 2006, Paper 174303. doi:10.1063/1.2186643

[28] Bose, D., and Wright, M., "Uncertainty Analysis of Laminar Aeroheating Predictions for Mars Entries," AIAA Paper 2005-4682, June 2005.

[29] Daiß, A., Frühauf, H.-H., and Messerschmid, E. W., "Chemical Reactions and Thermal Nonequilibrium on Silica Surfaces," *Molecular Physics and Hypersonic Flows*, edited by M. Capitelli, Kluwer Academic, Norwell, MA, 1996, pp. 203–218.

[30] Daiß, A., Frühauf, H.-H., and Messerschmid, E. W., "Modeling of Catalytic Reactions on Silica Surfaces with Consideration of Slip Effects," *Journal of Thermophysics and Heat Transfer*, Vol. 11, No. 3, 1997, pp. 346–352. doi:10.2514/2.6272

[31] Deutschmann, O., Riedel, U., and Warnatz, J., "Modeling of Nitrogen and Oxygen Recombination on Partial Catalytic Surfaces," *Journal of Heat Transfer*, Vol. 117, No. 2, May 1995, pp. 495–501. doi:10.1115/1.2822549

[32] Kovalev, V. L., Suslov, O. N., and Triskiy, G. A., "Phenomenological Theory for Heterogeneous Recombination of Partially Dissociated Air on High-Temperature Surfaces," *Molecular Physics and Hypersonic Flows*, edited by M. Capitelli, Kluwer Academic, Norwell, MA, 1996, pp. 193–202.

[33] Natsui, F., Barbato, M., and Bruno, C., "Material-Dependent Catalytic Recombination Modeling for Hypersonic Flows," *Journal of Thermophysics and Heat Transfer*, Vol. 10, No. 1, 1996, pp. 131–136. doi:10.2514/3.763

[34] Armenise, I., Barbato, M., Capitelli, M., and Kustova, E., "State-to-State Catalytic Models, Kinetics, and Transport in Hypersonic Boundary Layers," *Journal of Thermophysics and Heat Transfer*, Vol. 20, No. 3, 2006, pp. 465–476. doi:10.2514/1.18218